Chemo-mechanical benchmark for phase-field approaches

Thea Kannenberg[1,2,*] ⓘ**, Andreas Prahs**[1] ⓘ**,
Bob Svendsen**[3,4] ⓘ**, Britta Nestler**[1,2,5] ⓘ
and Daniel Schneider[2,5] ⓘ

[1] Karlsruhe Institute of Technology (KIT), Institute for Applied
Materials (IAM-MMS), Straße am Forum 7, 76131 Karlsruhe, Germany

[2] Karlsruhe University of Applied Sciences, Institute of Digital Materials
Science (IDM), Moltkestraße 30, 76133 Karlsruhe, Germany

[3] Max Planck Institute for Sustainable Materials, Microstructure Physics and Alloy
Design, Max-Planck-Straße 1, 40237 Düsseldorf, Germany

[4] RWTH Aachen University, Material Mechanics, Schinkelstraße 2, 52062 Aachen,
Germany

[5] Karlsruhe Institute of Technology (KIT), Institute of Nanotechnology (INT-MSS),
Hermann-von-Helmholtz-Platz 1, 76344 Eggenstein-Leopoldshafen, Germany

E-mail: thea.kannenberg@h-ka.de

Abstract
Phase-field approaches have gained increasing popularity as a consequence of
their ability to model complex coupled multi-physical problems. The efficient
modeling of migrating diffuse phase boundaries is a fundamental character-
istic. A notable advantage of phase-field methods is their ability to account for
diverse physical driving forces for interfacial motion due to diffusive, mech-
anical, electro-chemical, and other processes. As a result of this versatility,
phase-field methods are frequently employed in the fields of materials science,
mechanics, and physics, and are continually undergoing development. To test
the accuracy of these developments, it is indispensable to establish standard-
ized benchmark tests, to ensure the thermodynamic consistency of studies
carried out. This work presents a series of such tests based on chemo-elastic
equilibrium states for Fe-C binary alloys, benchmarking the performance of
a phase-field model with chemo-elastic coupling based on the grand potential

* Author to whom any correspondence should be addressed.

density. Use of parameters for the Fe-C system from a CALPHAD database allows for the determination of the Gibbs free energy, thereby enabling the quantification of chemical driving forces. For a circular inclusion, the capillary driving force is derived on a geometrically motivated basis using the lever rule and expressed as a function of the chemical potential. These simulations contribute to the development of standardized benchmark tests that validate chemical, capillary, and mechanical driving forces separately and in combination. The present study compares phase-field simulation results with results from the analytic solution of chemo-elastic boundary value problems and the generalized Gibbs–Thomson equation.

Keywords: phase-field approach, benchmark, chemo-elastic model

1. Introduction

Motivation. One of the primary objectives of materials science is the precise tailoring of materials with improved properties, such as high strength, light weight, and better sustainability. Modeling and simulation are powerful tools for predicting the behavior and characteristics of materials, making them indispensable in materials science. Furthermore, modeling and simulation can act as a bridge between theory and experiments. However, it should be ensured that the model used reflects the theoretical facts. For the simulation of phase transformation processes phase-field models are a widely used method. For an overview on phase-field models for microstructural evolution see e.g. [1–3]. The modeling of interfacial motion can be approached from a variety of perspectives, encompassing e.g. diffusive, mechanical, electro-chemical, and coupled processes. As a result, phase-field methods are constantly under development and it is therefore crucial to develop and establish standardized benchmark tests.

Phase-field method. A principal characteristic of phase-field models, see fundamental works [4–6], is the diffusiveness of interfaces, i.e. that interfaces between neighboring phases are described by a transition region of finite width. In the field of phase-field theory, the term *phase* is used not only to describe a phase in the thermodynamic sense as a distinct state dependent on temperature, composition, pressure, and so forth, but also to distinguish between grains of equal thermodynamic properties that exhibit, e.g. different orientations. Each phase is associated with a phase-field variable, the order parameter, which exhibits a continuous and steep transition between phases. From a microscopic perspective, the transition region of finite width can be attributed to the fact that the interfacial region is indeed characterized by an atomic arrangement different from the bulk within a spatially confined region. In mesoscopic phase-field models, the diffuse interface is rather a regularization of a singular surface that enables an efficient computation of moving boundaries due to the continuous nature of order parameters. One of the initial applications of the phase-field method was in the field of solidification [7]. Multiphase-field methods [8–10] were developed to overcome the restriction to two phases, allowing to model an arbitrary number of different phases or, in a polycrystalline framework, different grains of the same phase. Khachaturian's theory of microelasticity [11] constitutes an important contribution to the introduction of mechanics into phase-field models. A number of models have been developed that couple diffusive and displacive transformation processes, here so called chemo-mechanical models, e.g. [12]. Among the many applications of chemo-mechanical phase-field models recent research include the modeling of various phase transformations in steels (see [13, 14] for a review), including the growth of Widmanstätten ferrite [15, 16], pearlite [17], martensite [18, 19], and bainite [20, 21] to name just a few, phase

transformations in superalloys [22–24], and the modeling of battery materials [25, 26]. In these models, different assumptions are made concerning the mechanical and chemical fields in the diffuse interface. The Reuss-Sachs (RS) approximation states that the phase-inherent stresses $\boldsymbol{\sigma}^\alpha$ are locally equal, cf equation (1), which results in a harmonic interpolation of phase-inherent stiffnesses $\mathbb{C}^\alpha$ [27]. Within the Voigt-Taylor (VT) approximation on the other hand, phase-inherent strains $\boldsymbol{\varepsilon}^\alpha$ are locally equal, cf equation (2), which results in a linear interpolation of phase-inherent stresses and stiffnesses [27]. Khatchaturyan (KHA) introduced yet another interpolation of stiffnesses and eigenstrains within the interfacial region [11]. All three approaches have been compared in the context of a chemo-elasto-plastic phase-field model in the work of Ammar *et al* [27]. The jump condition approach accounts for the mechanical jump conditions in the sense that the balance of linear momentum on a material singular surface, i.e. the continuity of the stress vector normal to the interface $\boldsymbol{t} = \boldsymbol{\sigma} \boldsymbol{n}_S$, where $\boldsymbol{n}_S$ describes the interface normal, as well as the Hadamard condition are satisfied at each point within the diffuse interface, cf equation (3). Herein, the unknown jump vector and the normal vector between phases α and β are denoted by $\boldsymbol{a}^{\alpha\beta}$ and $\boldsymbol{n}^{\alpha\beta}$, respectively. A comparison of the jump condition approach (or similar homogenization approaches in the range of (partial) rank-one convexification) with VT and RS are conducted in [28–31]. In contrast to RS and VT, the jump approach is consistent with sharp interface modeling, see e.g. [32], which is an important aspect in the context of mesoscopic phase-field models. Otherwise, the interpolation assumption leads to excess energy within interfacial regions which in turn can result in high stresses and incorrect phase transformation kinetics. Regarding chemical heterogeneities, the approach developed by Wheeler, Boettinger, and McFadden (WBM) assumes equal concentrations c^α [33] while the Kim-Kim-Suzuki (KKS) [34] as well as the grand chemical potential (GCP) [35, 36] models assume equal chemical potentials μ^α within the diffuse interface region, cf equations (4) and (5). The WBM model involves an intrinsic coupling between bulk and interfacial free energy which results in a dependence of simulation results on interface thickness. As discussed in the context of mechanics, this becomes problematic for mesoscopic models where the width of the diffuse interface is well above the natural scale of diffuseness and thus, excess energy is introduced into the system. Both the KKS and the GCP models decouple bulk and interface contributions but differ in the choice of intrinsic variables. While the KKS model is based on the concentration field, the GCP model employs the chemical potential as evolving field quantity, see e.g. [35]. The performance of chemo-elastic coupling, specifically the combination of the GCP model with different mechanical homogenization schemes (RS, VT, KHA) has been discussed by Simon *et al* [37]. The introduction of both chemical and mechanical contributions to the system can impact the interfacial energy. To accurately model the interplay of coupled multi-physics with curvature driven phase transformations, it is necessary to preserve the physical interfacial energy, see e.g. [38]. The assumptions concerning the mechanical and chemical fields in the diffuse interface described above can be summarized as

$$\boldsymbol{\sigma} = \boldsymbol{\sigma}^\alpha = \boldsymbol{\sigma}^\beta \qquad \text{(RS [27])}, \qquad (1)$$

$$\boldsymbol{\varepsilon} = \boldsymbol{\varepsilon}^\alpha = \boldsymbol{\varepsilon}^\beta \qquad \text{(VT [27])}, \qquad (2)$$

$$\lbrace\!\lbrace \boldsymbol{t} \rbrace\!\rbrace^{\alpha\beta} = \boldsymbol{0}, \quad \lbrace\!\lbrace \boldsymbol{\varepsilon} \rbrace\!\rbrace^{\alpha\beta} = \frac{1}{2}\left(\boldsymbol{a}^{\alpha\beta} \otimes \boldsymbol{n}^{\alpha\beta} + \boldsymbol{n}^{\alpha\beta} \otimes \boldsymbol{a}^{\alpha\beta}\right) \qquad \text{(Jump [28–30, 39])}, \qquad (3)$$

$$c = c^\alpha = c^\beta \qquad \text{(WBM [33])}, \qquad (4)$$

$$\mu = \mu^\alpha = \mu^\beta \qquad \text{(KKS [34], GCP [35, 36])}. \qquad (5)$$

In the equations above, phase-dependent quantities are indicated by the superscripts α and β. Further notation conventions are introduced in the paragraph *Notation* at the end of this section.

In addition to different assumptions within the diffuse interface region, it is possible to distinguish between different modes of coupling, which may be interpreted as the type or degree of interaction between the stress and concentration field. A model is only considered fully coupled in a chemo-mechanical sense, if the stress field, and thus the displacement field, is impacted by the concentration and vice versa, which implies that the diffusion is dependent on the stress, e.g. [22]. Thus, a model is called chemo-mechanically weakly coupled, if the impact of the stress on the diffusion is neglected, as e.g. in [15]. The stress can be modeled concentration dependent e.g. by the introduction of concentration dependent elastic constants see e.g. [40], or concentration dependent eigenstrains see e.g. [22], in a weakly and fully coupled sense.

Benchmarks. Due to the wide range of chemo-mechanical phase-field models working with different assumptions and operating on different length scales, the development of standardized benchmark tests is an important task within the phase-field community. A comparison of models and implementations is enabled by a collection of standardized benchmarks [41]. Jokisaari *et al* [41] delineated fundamental requirements for benchmarks which include the targeting of varying degrees of computational complexity, while not necessitating extensive computational resources. Furthermore, simulation outputs which can be easily compared and quantified by the evolution of overall metrics such as system energy or phase fractions are aimed at. According to Jokisaari *et al* [41], benchmarks should either target numerical implementation (e.g. simple physics with complicated boundary conditions) or target physics (e.g. simple domain with coupled physics). Recently developed benchmarks within the phase-field community include benchmarks for numerical implementation [41], triple junction benchmarks for the construction of interfacial energy contributions [38, 42], to include anisotropy in a curvature-driven system [43], and benchmarks for linear elasticity [44]. Some benchmarks have also already been developed for chemo-mechanical phase-field models: Ammar *et al* [27] compared equilibrium concentrations and molar fractions with analytical Cahn-Larché solutions [45]. However, no curvature contributions are examined. Similarly, Durga *et al* [28] chose a setup without curvature for the comparison of different homogenizations schemes within the diffuse interface region. Durga *et al* [46] investigate a setup with an elliptic inclusion, however, its size is fixed and does not evolve corresponding to the concentration evolution. The concentration shift due to the curvature of the interface is calculated based on an 'effective circle radius'. Additionally, the analytical solution used for comparison is obtained for a matrix of infinite size. Simon *et al* [37] also work with a fixed size inclusion and do not investigate the equilibrium size influenced by the concentration at equilibrium. In the work by Kiefer *et al* [31] chemical energy contributions are constant and no evolution of concentrations is modeled. Bai *et al* [47] employed a chemo-mechanical model, the presented benchmark however is limited to the validation of chemical driving forces. The benchmark developed by Kamachali *et al* [40] addresses precipitation in the presence of chemo-mechanical coupling. The effect of elastic energy on the concentration is not considered in the derivation of the equilibrium concentration for a precipitate in a matrix. Furthermore, the impact of chemical, capillary, and mechanical driving forces is not analyzed separately within one benchmark. In the work by Tschukin *et al* [48], chemical forces are incorporated into the phase-field equation to overcome the quasi-equilibrium state between the elastic and capillary forces in the thermodynamic equilibrium and are thus adjusted for each setup.

Originality. Within the proposed benchmarks, Gibbs free energies are formulated using a parabolic approximation based on CALPHAD databases. Consequently, the chemical driving forces are formulated based on thermodynamic data and do not depend on the benchmark setup. An analytical solution to the equilibrium state of an inclusion in terms of the equilibrium chemical

potential is derived. Furthermore, an expression for the curvature of a circular inclusion in terms of the chemical potential is derived which is geometrically motivated and based on the lever rule, see e.g. [49]. Moreover, the analytical solution utilized for the mechanical driving force is derived for a finite section of an infinite plate. Therefore, the analytical solution can be directly compared to the phase-field simulation. In conclusion, the proposed setup allows for an analytical treatment of the chemical, capillary, and mechanical driving force. In contrast to the aforementioned chemo-mechanical benchmarks, the proposed framework allows for the validation of the influence of chemical, mechanical, and capillary driving forces separately and within a single benchmark. To this end, the evolution of order parameters and concentration is simulated until equilibrium is reached. The analytically derived capillary driving force is directly linked to the equilibrium composition and the equilibrium chemical potential, by utilizing the lever rule. This approach allows for the examination of the impact of a change in concentration on the capillary driving force. Any modification of the system's configuration will result in different driving forces and, consequently, a shift in the equilibrium chemical potential and equilibrium concentrations, which is reflected directly in the equilibrium phase fractions.

Objective. This paper contributes to the development of benchmarks for a chemo-mechanical phase-field model, in order to validate whether the interaction of diffusive, displacive, and curvature driven forces is accurately represented. A weakly coupled chemo-mechanical model is addressed following the derivation in [15], where the chemical driving forces can be derived based on a grand potential multiphase-field method [35, 36]. This model is chemo-mechanically weakly coupled, in the sense that the mechanical part of the free energy density does not directly depend on the concentration and the chemical free energy density does not directly depend on stresses or strains. The objective of the presented tests is to provide a benchmark example that allows for the validation of chemical, capillary, and mechanical driving forces and their interplay based on an equilibrium chemical potential. This enables the validation of the model implementation and facilitates comparison of different model assumptions. The proposed setup allows for the complexity to be increased gradually, thus enabling the benchmark to be used for solely chemical phase-field models or for combined validation within a single setup of chemo-mechanical models. In order to ascertain that the phase-field results yield consistent equilibrium conditions, they are quantitatively compared with the analytically derived equilibrium solutions based on the generalized Gibbs-Thomson equation. This guarantees that the mechanical fields, such as stress, displacement, and strain fields, as well as the concentration field in equilibrium are consistent with thermodynamic theory. The accuracy of different model assumptions can be evaluated and compared in terms of the equilibrium phase fractions, as demonstrated in the last benchmark example for three homogenization schemes with respect to the mechanical fields, namely RS, VT, and Jump.

Outline. The paper is organized as follows. In section 2, the basic model relations are summarized. The benchmark tests are described in the following sections: The analytical solution of the corresponding sharp interface solution is given in section 3, and the used parameters and results of the simulation are discussed in section 4. Finally, this work is concluded in section 5.

Notation. The following notations are used throughout this work: Scalars, vectors, 2nd-order, and 4th-order tensors are designated by a, $\boldsymbol{a}$, $\boldsymbol{A}$, and $\mathbb{A}$, respectively. A linear mapping of a vector by a 2nd-order tensor is denoted by $\boldsymbol{Ab}$, and the mapping of a 2nd-order tensor by a 4th-order tensor by $\mathbb{A}[\boldsymbol{B}]$. A composition is written as $\boldsymbol{AB}$, and the dyadic product is given by $\boldsymbol{a} \otimes \boldsymbol{b}$ and $\boldsymbol{A} \otimes \boldsymbol{B}$. Scalar products are written as $\boldsymbol{a} \cdot \boldsymbol{b}$, $\boldsymbol{A} \cdot \boldsymbol{B}$, and $\mathbb{A} \cdot \mathbb{B}$, respectively. The gradient of a scalar is expressed with the nabla operator as ∇a and the divergence of a 2nd-order tensor

as $\nabla \cdot \boldsymbol{A}$. The jump of a quantity ψ across a material singular surface $\mathcal{S}$ with corresponding limits ψ^+ and ψ^- within the two subvolumes $\mathcal{V}^+$ and $\mathcal{V}^-$ is written as $[\![\psi]\!] = \psi^+ - \psi^-$. The jump of a quantity ψ between phase α and β is defined analogously as $[\![\psi]\!]^{\alpha\beta} = \psi^\alpha - \psi^\beta$. The normal vector $\boldsymbol{n}_\mathcal{S}$ on $\mathcal{S}$ points from $\mathcal{V}^-$ to $\mathcal{V}^+$. The outward normal vectors on $\mathcal{V}^+$ and $\mathcal{V}^-$ are written as $\boldsymbol{n}_{\mathcal{V}+}$ and $\boldsymbol{n}_{\mathcal{V}-}$, respectively, and the relation $\boldsymbol{n}_\mathcal{S} = -\boldsymbol{n}_{\mathcal{V}+} = +\boldsymbol{n}_{\mathcal{V}-}$ holds true.

2. Model formulation

Functional. The free energy functional of Ginzburg–Landau type [5] describing the energy state of an isothermal chemo-elastic transformation process of two phases can be defined as

$$\mathcal{F}[\phi_\alpha, \bar{c}, \bar{\boldsymbol{\varepsilon}}] = \int_V [f_{\text{intf}}(\phi_\alpha, \nabla\phi_\alpha) + \bar{f}_{\text{chem}}(\phi_\alpha, \bar{c}) + \bar{f}_{\text{el}}(\phi_\alpha, \bar{\boldsymbol{\varepsilon}})]\,\mathrm{d}V. \tag{6}$$

Herein, ϕ_α is the order parameter of phase α and its gradient is denoted by $\nabla\phi_\alpha$. The model formulation to follow is based on the assumption

$$\phi_\alpha + \phi_\beta = 1, \tag{7}$$

i.e. the phase evolution can be described using only one independent order parameter ϕ_α and consequently $\phi_\beta = 1 - \phi_\alpha$. Each order parameter is related to the volume fraction of the respective phase. Additionally, in the two-phase case, $\nabla\phi_\beta = -\nabla\phi_\alpha$ holds true. The interfacial energy density $f_{\text{intf}}(\phi_\alpha, \nabla\phi_\alpha)$ with units $\mathrm{J\,m^{-3}}$ is additively composed of a gradient energy density $f_{\text{grad}}(\nabla\phi_\alpha)$ and a potential energy density $f_{\text{pot}}(\phi_\alpha)$,

$$f_{\text{intf}}(\phi_\alpha, \nabla\phi_\alpha) = f_{\text{pot}}(\phi_\alpha) + f_{\text{grad}}(\nabla\phi_\alpha). \tag{8}$$

The chemical free energy density $\bar{f}_{\text{chem}}$ and the elastic energy density $\bar{f}_{\text{el}}$ are given by linear interpolation of the corresponding phase-specific energy densities with units $\mathrm{J\,m^{-3}}$

$$\bar{f}_{\text{chem}} = \phi_\alpha f_{\text{chem}}^\alpha + (1 - \phi_\alpha) f_{\text{chem}}^\beta, \quad \bar{f}_{\text{el}} = \phi_\alpha f_{\text{el}}^\alpha + (1 - \phi_\alpha) f_{\text{el}}^\beta. \tag{9}$$

A discussion on the kinetics of triple junctions with additional bulk driving forces employing a multiphase-field approach can be found in [50].

Evolution equation of order parameters. The phase transformation governed by elastic and chemical free energy densities is modeled as an interaction of the two phases as introduced in [3, 9]. The evolution equation of order parameters reads

$$\frac{\partial\phi_\alpha}{\partial t} = -\frac{M_{\alpha\beta}}{2\epsilon}\left(\frac{\delta f_{\text{intf}}}{\delta\phi_\alpha} - \frac{\delta f_{\text{intf}}}{\delta\phi_\beta} + \frac{8\sqrt{\phi_\alpha(1-\phi_\alpha)}}{\pi}\Delta_{\text{bulk}}^{\alpha\beta}\right). \tag{10}$$

The chemical and mechanical bulk driving forces $\Delta_{\text{chem}}^{\alpha\beta}$ and $\Delta_{\text{mech}}^{\alpha\beta}$, respectively, constitute the total bulk driving force $\Delta_{\text{bulk}}^{\alpha\beta}$ by addition, i.e. $\Delta_{\text{bulk}}^{\alpha\beta} = \Delta_{\text{chem}}^{\alpha\beta} + \Delta_{\text{mech}}^{\alpha\beta}$, and are defined as $(\delta/\delta\phi_\alpha - \delta/\delta\phi_\beta)\bar{f}_{\text{chem}}$ and $(\delta/\delta\phi_\alpha - \delta/\delta\phi_\beta)\bar{f}_{\text{el}}$. Corresponding to the free energy densities defined in equations (18)–(20), (24) the variational derivative

$$\frac{\delta(\cdot)}{\delta\phi_\alpha} = \frac{\partial(\cdot)}{\partial\phi_\alpha} - \nabla\cdot\frac{\partial(\cdot)}{\partial\nabla\phi_\alpha} \tag{11}$$

see e.g. [51, equation (13.63)] is used. The parameter $M_{\alpha\beta}$ denotes the mobility between phases α and β. The width of the interface can be adjusted with the parameter ϵ.

Chemical driving force. The benchmark cases considered are restricted to two components A and B, i.e. the corresponding unit-less mole fractions (also referred to as atomic fractions) satisfy $\bar{c}_A + \bar{c}_B = 1$. Thus, the system can be described with only one independent component $\bar{c}_A = \bar{c}$. The mole fractions of phases α and β are described by c^α and c^β, respectively. The interpolation relation of the independent component $\bar{c}$ reads

$$\bar{c} = \phi_\alpha c^\alpha + (1 - \phi_\alpha) c^\beta. \tag{12}$$

Equal phase chemical potentials within the diffuse interface are considered, cf equation (5), with

$$\mu^\alpha := \frac{\partial f_{\text{chem}}^\alpha}{\partial c^\alpha}, \tag{13}$$

see e.g. [36]. Assuming a constant molar volume V_{m} which is independent of phases, i.e.

$$V_{\text{m}} = V_{\text{m}}^\alpha = V_{\text{m}}^\beta, \tag{14}$$

the chemical potential μ with units J m^{-3} is related to the molar chemical potential $\tilde{\mu}$ with units J mol^{-1} through $\mu = \tilde{\mu}/V_{\text{m}}$. A similar definition is used, e.g. in [52, 53]. Considering the assumptions above, the chemical driving force follows as

$$\Delta_{\text{chem}}^{\alpha\beta} = \frac{\delta \bar{f}_{\text{chem}}}{\delta \phi_\alpha} - \frac{\delta \bar{f}_{\text{chem}}}{\delta \phi_\beta} \tag{15}$$

$$= f_{\text{chem}}^\alpha (c^\alpha) - \mu c^\alpha - \left(f_{\text{chem}}^\beta (c^\beta) - \mu c^\beta \right) \tag{16}$$

$$= \llbracket f_{\text{chem}} \rrbracket^{\alpha\beta} - \mu \llbracket c \rrbracket^{\alpha\beta}. \tag{17}$$

For a detailed derivation the reader is referred to [15, 36]. Accounting for equation (14), the Gibbs and the Helmholtz free energy density, G^α and f_{chem}^α, respectively, are related through $f_{\text{chem}}^\alpha(c^\alpha) = G^\alpha(c^\alpha)/V_{\text{m}}$. Employing a parabolic approximation and considering an isothermal system, the chemical free energy density of phase α can be modeled as

$$f_{\text{chem}}^\alpha (c^\alpha) = \frac{1}{V_{\text{m}}} \left(A^\alpha (c^\alpha)^2 + B^\alpha c^\alpha + C^\alpha \right), \tag{18}$$

allowing for an efficient computation. The coefficients A^α, B^α, and C^α are of unit J mol^{-1}. In this work, the CALPHAD database TCFE7 for the Fe-C system from the Thermo-Calc software [54] is used. An example workflow for the incorporation of CALPHAD data from the Thermo-Calc software using parabolic approximations, is described in detail in [55]. The functions, i.e. the coefficients are fitted using a least-square approach.

Capillary driving force. A gradient energy density for two phases as proposed in [9]

$$f_{\text{grad}} (\nabla \phi_\alpha) = \epsilon \gamma_{\alpha\beta} \nabla \phi_\alpha \cdot \nabla \phi_\alpha \tag{19}$$

is used. The interfacial energy is written as $\gamma_{\alpha\beta}$ and is assumed to be isotropic. The width of the interface in equilibrium l_{eq} is given by $l_{\text{eq}} = \epsilon\pi^2/4$. The multi-obstacle potential is given by

$$f_{\text{pot}}(\phi_\alpha) = \frac{16}{\epsilon\pi^2}\gamma_{\alpha\beta}\phi_\alpha(1-\phi_\alpha) \tag{20}$$

see [10]. It is set to ∞ if the order parameters ϕ_α and ϕ_β are not within the Gibbs simplex,

$$\mathcal{G} = \left\{ \boldsymbol{\phi} : \sum_{\alpha=1}^{2}\phi_\alpha(\boldsymbol{x},t) = 1, \phi_\alpha \geqslant 0 \right\}. \tag{21}$$

The interfacial contribution in the evolution equation of order parameters introduced in equation (10) reads

$$\frac{\delta f_{\text{intf}}}{\delta\phi_\alpha} - \frac{\delta f_{\text{intf}}}{\delta\phi_\beta} = \frac{16}{\epsilon\pi^2}\gamma_{\alpha\beta}(1-2\phi_\alpha) - 2\epsilon\gamma_{\alpha\beta}\triangle\phi_\alpha, \tag{22}$$

where $\triangle = \nabla \cdot \nabla$ denotes the Laplace operator.

Mechanical driving force. The derivation of the mechanical bulk driving force $\Delta_{\text{mech}}^{\alpha\beta}$, which is solely elastic in this work, is determined by adopting an approach presented in [30, 39, 56]. This method accounts for the mechanical jump conditions in the sense that the balance of linear momentum on a material singular surface as well as the Hadamard condition are satisfied at each point within the diffuse interface, cf equation (3). Within this work a small strain framework is considered, i.e. the infinitesimal strain $\bar{\varepsilon}$ is related to the continuous displacement field $\boldsymbol{u}$ via $\bar{\varepsilon} = (\nabla\boldsymbol{u} + (\nabla\boldsymbol{u})^{\mathsf{T}})/2$. The resulting mechanical driving force is written as

$$\Delta_{\text{mech}}^{\alpha\beta} = [\![f_{\text{el}}]\!]^{\alpha\beta} - \bar{\boldsymbol{\sigma}} \cdot [\![\varepsilon]\!]^{\alpha\beta}. \tag{23}$$

Herein, the phase-specific elastic energy densities are given by

$$f_{\text{el}}^\alpha = \frac{1}{2}\left(\varepsilon^\alpha \cdot \mathbb{C}^\alpha[\varepsilon^\alpha]\right) \tag{24}$$

and the interpolated stress tensor is defined as $\bar{\boldsymbol{\sigma}} = \sum_{\alpha=1}^{N}\phi_\alpha\boldsymbol{\sigma}^\alpha$, see e.g. [39].

Evolution equation of concentration and chemical potential. The evolution equation of concentration is given by

$$\frac{\partial\bar{c}}{\partial t} = \nabla \cdot (\bar{M}(\phi_\alpha)\nabla\mu), \tag{25}$$

where the mobility comprises of the phase-specific mobilities $\bar{M}(\phi_\alpha) = \phi_\alpha M^\alpha + (1-\phi_\alpha)M^\beta$. According to, e.g., Choudhury and Nestler [36, equations (22)–(24)], each phase-specific mobility depends on the diffusivity D^α of the independent component in phase α

$$M^\alpha = D^\alpha\frac{\partial c^\alpha(\mu)}{\partial\mu}. \tag{26}$$

The evolution equation of the chemical potential follows from equations (12) and (25)

$$\frac{\partial \mu}{\partial t} = \left[\phi_\alpha \frac{\partial c^\alpha(\mu)}{\partial \mu} + (1 - \phi_\alpha) \frac{\partial c^\beta(\mu)}{\partial \mu} \right]^{-1} \left(\nabla \cdot \bar{M}(\phi_\alpha) \nabla \mu - \left(c^\alpha(\mu) - c^\beta(\mu) \right) \frac{\partial \phi_\alpha}{\partial t} \right),$$
(27)

see [36, equation (26)], which is computationally efficient.

3. Analytics

Equilibrium conditions. In this work, simulative results in the diffuse interface context are compared with analytic solutions based on equilibrium properties for sharp interfaces given by the generalized Gibbs-Thomson equation for two phases α and β

$$\lfloor \omega \rceil^{\alpha\beta} - \bar{\boldsymbol{\sigma}} \cdot \lfloor \boldsymbol{\varepsilon} \rceil^{\alpha\beta} = -2\Gamma \bar{\kappa}_{\mathcal{S}},$$
(28)

see e.g. [57, 58], where $\bar{\kappa}_{\mathcal{S}}$ describes the mean curvature of the interface, cf equation (35). Herein, $+ \equiv \alpha$ and $- \equiv \beta$ is assumed regarding the subvolumes introduced in section 1, and thus $\boldsymbol{n}_{\mathcal{S}} = -\boldsymbol{n}^\alpha$. In the sharp interface context the mean stress is given by $\bar{\boldsymbol{\sigma}} = (\boldsymbol{\sigma}^\alpha + \boldsymbol{\sigma}^\beta)/2$, see e.g. [32, p 32]. Furthermore, ω and Γ denote the grand canonical energy density and the surface excess grand canonical energy density, respectively.

Approach for a binary two-phase system. In the following, three setups are introduced benchmarking chemical, capillary, and mechanical bulk driving forces. Firstly, only chemical driving forces are considered, in a second benchmark capillary effects are included, and lastly chemical, mechanical, and capillary driving forces are combined in one setup. This step-by-step procedure incrementally increases the complexity of the benchmarks. A uniform approach is proposed for all benchmarks in order to derive the analytical sharp solution needed for comparison with simulative results:

(i) Define domain and boundaries.
(ii) Formulate the volumetric driving force $\Delta^{\alpha\beta}(\mu)$ in terms of the chemical potential μ.
(iii) Solve equilibrium condition $\Delta^{\alpha\beta}(\mu) = 0$ for equilibrium chemical potential μ_{eq}.
(iv) Compute equilibrium concentration $c_{\text{eq}}^\alpha(\mu_{\text{eq}})$ and $c_{\text{eq}}^\beta(\mu_{\text{eq}})$.
(v) Define overall concentration c_{tot}.
(vi) Compute equilibrium phase fractions $\xi_{\text{eq}}^\alpha(c_{\text{eq}}^{\alpha,\beta})$ and $\xi_{\text{eq}}^\beta(c_{\text{eq}}^{\alpha,\beta})$ with lever rule.

3.1. Setup I — chemical driving forces

Equilibrium condition. In this first setup, only chemical driving forces $\Delta_{\text{chem}}^{\alpha\beta}$ are considered. Thus, the jump of the grand canonical energy densities, introduced in equation (28), is given by

$$\lfloor \omega \rceil^{\alpha\beta} = \lfloor \Psi \rceil^{\alpha\beta},$$
(29)

i.e. it reduces to the jump of the grand chemical potentials at the sharp interface as introduced in equation (17) with $\Psi^\alpha = f_{\text{chem}}^\alpha - \mu c^\alpha$. Thus, for a purely chemical system with flat interfaces, i.e. $\bar{\kappa}_{\mathcal{S}} = 0$, the equilibrium condition reads

$$\Delta^{\alpha\beta}(\mu) = \Delta_{\text{chem}}^{\alpha\beta}(\mu) = \lfloor \Psi \rceil^{\alpha\beta} = 0.$$
(30)
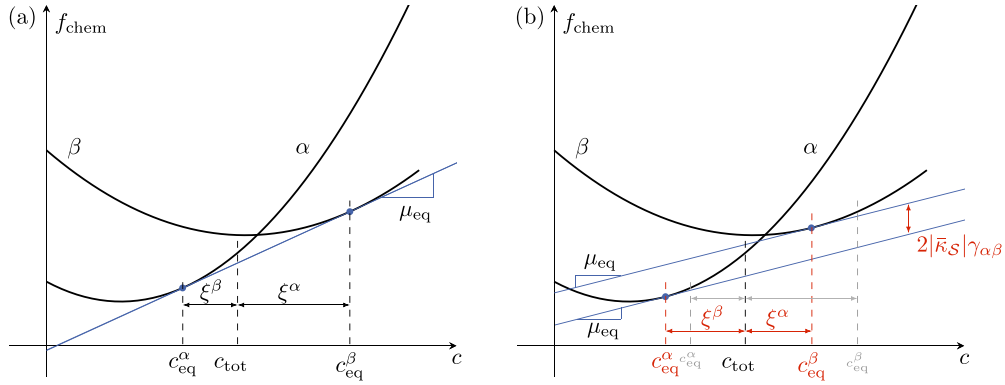
Figure 1. Schematic depiction of the Gibbs energy of two phases α and β in equilibrium. Without curvature contribution the equilibrium state is characterized by a common tangent (a), and with curvature contribution the equilibrium state is characterized by parallel tangents (b).

Within this first setup, the driving force $\Delta^{\alpha\beta}(\mu)$ is the chemical driving force for a two-phase binary system, which reads

$$\Delta^{\alpha\beta}(\mu) = \mu^2 V_{\mathrm{m}} \left(\frac{1}{4A^\beta} - \frac{1}{4A^\alpha} \right) + \mu \left(\frac{B^\alpha}{2A^\alpha} - \frac{B^\beta}{2A^\beta} \right) + \frac{1}{V_{\mathrm{m}}} \left(-\frac{(B^\alpha)^2}{4A^\alpha} + \frac{(B^\beta)^2}{4A^\beta} + C^\alpha - C^\beta \right) \tag{31}$$

employing equation (18). The inversion of the expression for the chemical potential $\mu(c^\alpha) = (2A^\alpha c^\alpha + B^\alpha)/V_{\mathrm{m}}$ (cf equations (13) and (18)) used in the derivation above yields the phase specific concentrations

$$c^\alpha(\mu) = \frac{\mu V_{\mathrm{m}} - B^\alpha}{2A^\alpha}, \quad c^\beta(\mu) = \frac{\mu V_{\mathrm{m}} - B^\beta}{2A^\beta}, \tag{32}$$

which are needed to compute phase fractions $\xi^{\alpha,\beta}$ using the lever rule, see e.g. [49],

$$\xi^\alpha = \frac{|c^\beta(\mu) - c_{\mathrm{tot}}|}{|c^\beta(\mu) - c^\alpha(\mu)|}, \quad \xi^\beta = \frac{|c^\alpha(\mu) - c_{\mathrm{tot}}|}{|c^\beta(\mu) - c^\alpha(\mu)|}. \tag{33}$$

A schematic depiction of the equilibrium state, characterized by the common tangent with slope μ_{eq}, the equilibrium compositions c_{eq}^α and c_{eq}^β, and the corresponding phase fractions ξ^α and ξ^β given by the lever rule is provided in figure 1(a).

3.2. Setup II — chemical and capillary driving forces

Equilibrium condition. In this second setup, a system with a curved interface is considered, i.e. $\bar{\kappa}_{\mathcal{S}} \neq 0$. Thus, capillary driving forces are introduced into the system. The capillary driving force $\Delta_{\mathrm{cap}}^{\alpha\beta}$ is derived from equation (22) and written as

$$\Delta_{\mathrm{cap}}^{\alpha\beta} = 2\bar{\kappa}_{\mathcal{S}} \gamma_{\alpha\beta}. \tag{34}$$

In general, the mean curvature of a singular surface is given by

$$\bar{\kappa}_{\mathcal{S}} = -\frac{\nabla_{\mathcal{S}} \cdot \boldsymbol{n}_{\mathcal{S}}}{2}, \tag{35}$$

see e.g. [59, equation (2.2)]. In the equation above, the mean curvature of a singular surface $\bar{\kappa}_{\mathcal{S}}$ is expressed in terms of the interface normal $\boldsymbol{n}_{\mathcal{S}}$. The equilibrium condition, combining chemical driving forces $\Delta_{\text{chem}}^{\alpha\beta}$ and capillary driving forces $\Delta_{\text{cap}}^{\alpha\beta}$, is given by

$$\Delta^{\alpha\beta}(\mu) = \Delta_{\text{chem}}^{\alpha\beta}(\mu) + \Delta_{\text{cap}}^{\alpha\beta}(\mu) = \{\Psi\}^{\alpha\beta} + 2\bar{\kappa}_{\mathcal{S}}\gamma_{\alpha\beta} = 0. \tag{36}$$

The additional capillary driving force causes a shift of the equilibrium composition and phase fractions as schematically depicted in figure 1(b). To examine this setup with the approach described above, the curvature $\bar{\kappa}_{\mathcal{S}}$ has to be expressed as a function of the chemical potential, i.e. $\bar{\kappa}_{\mathcal{S}} = f(\mu)$. The equilibrium condition for such a system reads

$$\begin{aligned}
\Delta^{\alpha\beta}(\mu) = {}& \mu^2 V_{\text{m}} \left(\frac{1}{4A^{\beta}} - \frac{1}{4A^{\alpha}} \right) + \mu \left(\frac{B^{\alpha}}{2A^{\alpha}} - \frac{B^{\beta}}{2A^{\beta}} \right) \\
& + \frac{1}{V_{\text{m}}} \left(-\frac{(B^{\alpha})^2}{4A^{\alpha}} + \frac{(B^{\beta})^2}{4A^{\beta}} + C^{\alpha} - C^{\beta} \right) + 2\gamma_{\alpha\beta}\bar{\kappa}_{\mathcal{S}}(\mu).
\end{aligned} \tag{37}$$

3.3. Setup III — chemical, capillary, and mechanical driving forces

Equilibrium condition. Finally, mechanical loading is added to the preceding setup. Considering chemical, capillary, and mechanical driving forces, $\Delta_{\text{chem}}^{\alpha\beta}$, $\Delta_{\text{cap}}^{\alpha\beta}$, and $\Delta_{\text{mech}}^{\alpha\beta}$, respectively, the jump of the grand canonical energy density introduced in equation (28) is given by the jump of the grand chemical potential and the jump of the elastic energy density

$$\{\omega\}^{\alpha\beta} = \{\Psi\}^{\alpha\beta} + \{f_{\text{el}}\}^{\alpha\beta}. \tag{38}$$

Consequently, the equilibrium condition is given by

$$\begin{aligned}
\Delta^{\alpha\beta}(\mu) &= \Delta_{\text{chem}}^{\alpha\beta}(\mu) + \Delta_{\text{cap}}^{\alpha\beta}(\mu) + \Delta_{\text{mech}}^{\alpha\beta}(\mu) \\
&= \{\Psi\}^{\alpha\beta} + 2\bar{\kappa}_{\mathcal{S}}\gamma_{\alpha\beta} + \{f_{\text{el}}\}^{\alpha\beta} - \bar{\boldsymbol{\sigma}} \cdot \{\varepsilon\}^{\alpha\beta} = 0.
\end{aligned} \tag{39}$$

Additionally, the balance of linear momentum $\nabla \cdot \bar{\boldsymbol{\sigma}} = \boldsymbol{0}$ is solved for the displacement field $\boldsymbol{u}$. Within this chemo-mechanically weakly coupled model, the mechanical driving force $\Delta_{\text{mech}}^{\alpha\beta}$ is independent of the chemical potential. Thus, the driving force reads

$$\begin{aligned}
\Delta^{\alpha\beta}(\mu) = {}& \mu^2 V_{\text{m}} \left(\frac{1}{4A^{\beta}} - \frac{1}{4A^{\alpha}} \right) + \mu \left(\frac{B^{\alpha}}{2A^{\alpha}} - \frac{B^{\beta}}{2A^{\beta}} \right) \\
& + \frac{1}{V_{\text{m}}} \left(-\frac{(B^{\alpha})^2}{4A^{\alpha}} + \frac{(B^{\beta})^2}{4A^{\beta}} + C^{\alpha} - C^{\beta} \right) + 2\gamma_{\alpha\beta}\bar{\kappa}_{\mathcal{S}}(\mu) \\
& + \{f_{\text{el}}\}^{\alpha\beta} - \bar{\boldsymbol{\sigma}} \cdot \{\varepsilon\}^{\alpha\beta},
\end{aligned} \tag{40}$$

for a general domain.
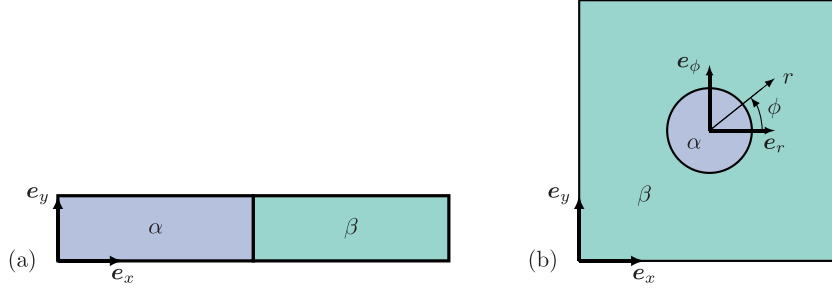
Figure 2. Initial domain with a flat interface corresponding to setup I (a) and a curved interface corresponding to setup II and III (b). The phases α and β correspond to an austenitic phase and a ferritic phase, respectively.

4. Simulation studies

Objective. The subsequent benchmark problems examine the impact of the different contributions to the free energy density defined in equation (6), namely the chemical, capillary, and mechanical energy density, on the equilibrium configuration of a two-phase domain. Three boundary value problems (BVPs) are defined, each specifying the equilibrium conditions of one setup derived in the preceding section for a general case. Simulations are conducted until an equilibrium state is reached. The equilibrium concentrations $c_{\mathrm{eq}}^{\alpha,\beta}$ and the equilibrium phase fraction $\xi_{\mathrm{eq}}^{\alpha,\beta}$ of the matrix and the inclusion are chosen as comparable simulation output. All phase-field simulations including the mechanics were run using the Pace3D in-house simulation software [60].

4.1. Simulation setup

Domain. For the first benchmark, corresponding to the setup I introduced in section 3.1, a quasi one-dimensional beam is discretized using an equidistant grid with 150×7 cells. The initial configuration is displayed in figure 2(a). Two phases α and β are separated by a flat interface, i.e. $\bar{\kappa}_{\mathcal{S}} = 0$. For the second and third benchmark, corresponding to setup II and III as introduced in sections 3.2 and 3.3, a circular inclusion α within a matrix β is considered. The domain is discretized with 200×200 cells if not otherwise specified, and is illustrated in figure 2(b). For all setups, if not otherwise specified, a spatial discretization $\Delta x = \Delta y = 2$ nm is used and the diffuse interface is discretized with $n_{\mathrm{I}} = 8$ cells. The interface is initialized exhibiting an equilibrium profile and width, i.e. $l_{\mathrm{eq}} = n_{\mathrm{I}} \Delta x = \epsilon \pi^2/4$. In order to specify the mean curvature $\bar{\kappa}_{\mathcal{S}}$, defined in equation (35), $\boldsymbol{n}_{\mathcal{S}} = -\boldsymbol{n}^{\alpha}$ is assumed as pointed out above. Thus, for the second and third benchmark involving a circular inclusion with radius a it follows

$$\bar{\kappa}_{\mathcal{S}} = -\frac{\nabla \cdot \boldsymbol{n}_{\mathcal{S}}}{2} = \frac{\nabla \cdot \boldsymbol{n}^{\alpha}}{2} = \frac{\nabla \cdot \boldsymbol{e}_r}{2} = \frac{1}{2a}. \tag{41}$$

Thus, employing the concentration equation (32) and the phase fraction equation (33) in terms of the chemical potential μ the mean curvature of the interface between inclusion α and matrix β can be expressed as

Table 1. Coefficients used for the parabolic approximation of the chemical free energy fitted at $T = 980\,\text{K}$ with the Thermo-Calc [54] TCFE7 CALPHAD database.

Coefficient	Ferrite	Austenite
A in $\text{J}\,\text{mol}^{-1}$	5829 166.667	162 958.333
B in $\text{J}\,\text{mol}^{-1}$	22 520.208	20 071.083
C in $\text{J}\,\text{mol}^{-1}$	−40 946.873	−40 680.599

Table 2. Material parameters.

Description	Symbol	Unit	Ferrite	Austenite	
Young's modulus	E	GPa	130	13	[15]
Poisson's ratio	ν	—	0.33	0.33	[15]
Diffusivity	D	$\text{m}^2\,\text{s}^{-1}$	2×10^{-9}	1×10^{-9}	[15]
Equilibrium concentration of carbon	c_{eq}	at.-%	0.097 4420	4.093 42	TCFE7
Molar volume	V_{m}	$\text{m}^3\,\text{mol}^{-1}$	7×10^{-6}	7×10^{-6}	[15]
Interfacial energy	$\gamma_{\alpha\beta}$	$\text{J}\,\text{m}^{-2}$	0.2		[15]
Mobility	$M_{\alpha\beta}$	$\text{m}^4\,\text{J}^{-1}\,\text{s}^{-1}$	1×10^{-11}		

$$\bar{\kappa}_{\mathcal{S}}\left(\mu\right) = \frac{1}{2a\left(\mu\right)} = \frac{1}{2}\left(\frac{\left|c_{\text{tot}} - \dfrac{\mu V_{\text{m}} - B^{\beta}}{2A^{\beta}}\right|}{\left|\dfrac{\mu V_{\text{m}} - B^{\beta}}{2A^{\beta}} - \dfrac{\mu V_{\text{m}} - B^{\alpha}}{2A^{\alpha}}\right|}\frac{A_{\text{tot}}}{\pi}\right)^{-\frac{1}{2}}. \tag{42}$$

Herein, the radius a of the inclusion α is written in terms of its phase fraction ξ^{α}, which depends on the chemical potential μ, i.e. $a = \sqrt{\xi^{\alpha}(\mu)A_{\text{tot}}/\pi}$. A_{tot} describes the total area of the simulation domain. Equation (42) constitutes a geometrically motivated criterion for the curvature of a circular inclusion based on the lever rule as a function of the chemical potential μ.

Material parameters. The presented benchmarks are applied to a binary system of carbon (C) and iron (Fe), where carbon is the independent component $\bar{c}$. The two phases are a ferritic phase (right bar, matrix, β) and an austenitic phase (left bar, inclusion, α). The fitted coefficients (obtained using the TCFE7 database of the Thermo-Calc software [54]) corresponding to equation (18) at $T = 980\,\text{K}$ are summarized in table 1. A least-square-method has been employed to fit the coefficients. Material parameters are summarized in table 2. It should be noted that the Young's modulus of the austenitic phase E^{aust} is formulated dependent on the Young's modulus of the ferritic phase, i.e. $E^{\text{aust}} = 0.1E^{\text{ferr}}$, in order to highlight the influence of the different stiffnesses. However, it is not representative for austenite. Since the transformation kinetics are not the focus of this work, the mobility $M_{\alpha\beta}$ is set to a constant value which ensures that the simulations run numerically stable.

Boundary conditions. In all benchmarks, zero-flux b oundary c onditions a re i mposed for the concentration at the domain boundary, thereby defining a n e nclosed s ystem wherein the average carbon content c_{tot} remains constant. In the quasi one-dimensional configuration (cf figure 2 (a)), t he z ero-gradient b oundary c ondition a pplied t o t he o rder parameters ensures that the interface remains perpendicular to the boundary during phase
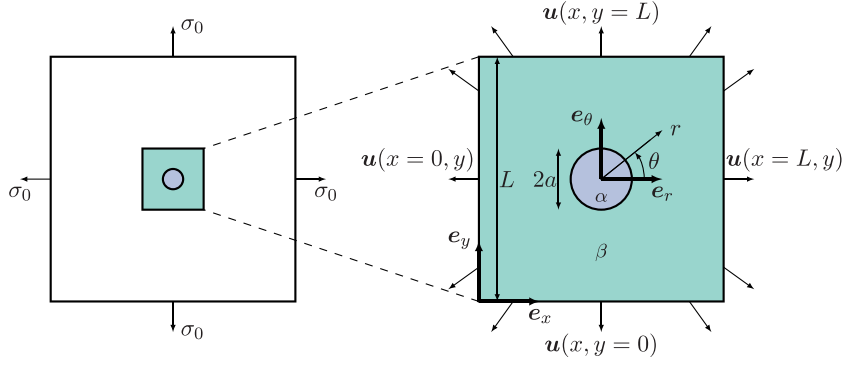
Figure 3. A two-dimensional plate subjected to hydrostatic tension σ_0 at infinity is constructed (left). A section of finite dimensions with length L is considered (right) with the corresponding Dirichlet boundary conditions. The inclusion and matrix are denoted by α and β, respectively.

evolution thereby emulating a one-dimensional setup. In the matrix-inclusion configuration (cf figures 2(b) and 3), the interface is not in contact with the domain boundary, as only smaller inclusions are examined, i.e. $2a < L$. In consequence, the boundary condition on the order parameters ensures a constant value at the boundary. For the third setup, a two-dimensional plate subjected to hydrostatic tension σ_0 at infinity and under plane strain conditions with a soft circular inclusion in its center is examined. A section of finite dimensions is considered as simulation domain, cf figure 3. From the analytical solutions for the described BVP, see [61], the displacement vector $\boldsymbol{u}(r)$ is derived as

$$\boldsymbol{u}\left(r\right) = \left(\frac{\sigma_0 r}{2\left(\lambda_\beta + G_\beta\right)} + \frac{\sigma_0 a^2 \left(\lambda_\beta + G_\beta - \lambda_\alpha - G_\alpha\right)}{2r\left(\lambda_\beta + G_\beta\right)\left(\lambda_\alpha + G_\alpha + G_\beta\right)} \right) \boldsymbol{e}_r \tag{43}$$

see [61, p 179]. For each simulation, the radius a in equation (43) is set to the equilibrium radius calculated with the sharp interface solution. Regarding benchmark III, the displacement vector $\boldsymbol{u}$ introduced in equation (43) is enforced on all boundaries, as schematically depicted in figure 3. Consequently, the mechanical driving force, cf equation (23), reads,

$$\left(\Delta_{\text{mech}}^{\alpha\beta}\right)_{\text{Mal}} = \frac{1}{2}\left(\sigma_{rr}^\alpha \varepsilon_{rr}^\beta + \sigma_{\theta\theta}^\alpha \varepsilon_{\theta\theta}^\beta - \sigma_{rr}^\beta \varepsilon_{rr}^\alpha - \sigma_{\theta\theta}^\beta \varepsilon_{\theta\theta}^\alpha \right) \tag{44}$$

$$= \frac{\sigma_0^2 \left(\lambda_\alpha + G_\alpha - \lambda_\beta - G_\beta\right)\left(\lambda_\beta + 2G_\beta\right)}{2\left(\lambda_\alpha + G_\alpha + G_\beta\right)\left(\lambda_\beta + G_\beta\right)^2} \tag{45}$$

see [61, pp 179–81]. Herein, σ_{rr}, $\sigma_{\theta\theta}$, ε_{rr}, and $\varepsilon_{\theta\theta}$ correspond to the solutions at the interface $(r = a)$ in radial and tangential direction derived by Mal [61], and $\lambda_{\alpha,\beta}$ and $G_{\alpha,\beta}$ denote the first Lamè constant and the shear modulus of the respective phases.

4.2. Results and discussion

Remark. In the following evaluations, phase fractions ξ^α resulting from the analytical solution were determined using the lever rule, cf equation (33). The phase fractions resulting from

the phase-field simulations (PFS) were calculated using $\xi^\alpha = \int_\Omega \phi_\alpha \mathrm{d}\, V / (\int_\Omega \mathrm{d}\, V)$. To ensure consistency with the lever rule, the equilibrium concentrations and phase fractions resulting
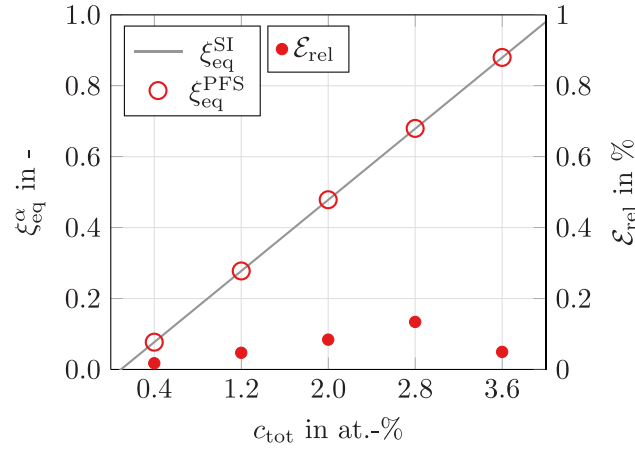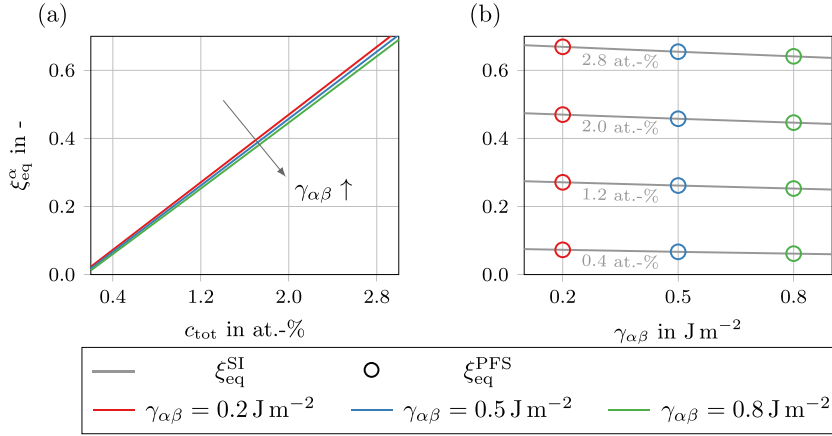
Figure 4. Benchmark I: the phase fractions resulting from the analytical sharp interface (SI) derivation described in setup I, where only chemical driving forces are considered, are compared with the results of the corresponding phase-field simulations (PFS). Phase fractions are displayed with respect to the left ordinate. The relative error of PFS results with respect to SI derivations ($\mathcal{E}_{\text{rel}}$) are illustrated referencing to the right ordinate.

from the PFS are compared with the classical lever rule predictions. The absolute deviation is less than 0.0007% in all PFS. Thus, the validation of equilibrium concentration through the use of equilibrium phase fractions is a justifiable approach.

Benchmark I — chemical driving forces. The equilibrium phase fractions ξ_{eq}^{α} which are calculated based on an analytical solution derived on the basis of approximated functions of the Gibbs energies constitute sharp interface (SI) solutions, cf equation (30). These SI solutions and the results of the PFS are compared and visualized in figure 4. In all of the following results, SI solutions are represented by solid lines and each unfilled mark represents a PFS result, both corresponding to the left ordinate. Furthermore, each filled mark represents an error and corresponds to the right ordinate. In this first benchmark, only chemical driving forces $\Delta_{\text{chem}}^{\alpha\beta}$ are accounted for corresponding to the first setup described in section 3.1. The total concentration c_{tot} is varied between the equilibrium concentrations predicted by the Thermo-Calc calculations. Perhaps not surprisingly, the closer the total concentration is to the equilibrium concentration of a phase, the larger the phase fraction of that phase. A good agreement of the PFS with respect to the SI solution is clearly visible. A direct comparison of PFS results with Thermo-Calc equilibrium calculations is not meaningful, as based on the deviation between these two datasets the error introduced by approximating the Gibbs energies cannot be separated from the error introduced by the phase-field simulation. The accuracy of the parabolic approximation is further discussed in appendix A. The small error $\mathcal{E}_{\text{rel}}$, describing the relative error of PFS with respect to SI, indicates a high precision of the phase-field simulations. This first benchmark setup for chemical driving forces is analogous to the benchmark presented by Bai *et al* [47] and is solely intended for the validation of chemical driving forces.

Benchmark II — chemical and capillary driving forces. In a second benchmark, the chemical driving forces $\Delta_{\text{chem}}^{\alpha\beta}$ are validated in combination with capillary driving forces $\Delta_{\text{cap}}^{\alpha\beta}$ as introduced in Setup II, cf section 3.2. For this purpose the equilibrium size of an inclusion within a matrix is examined as described above. The resulting equilibrium phase fractions ξ_{eq} are
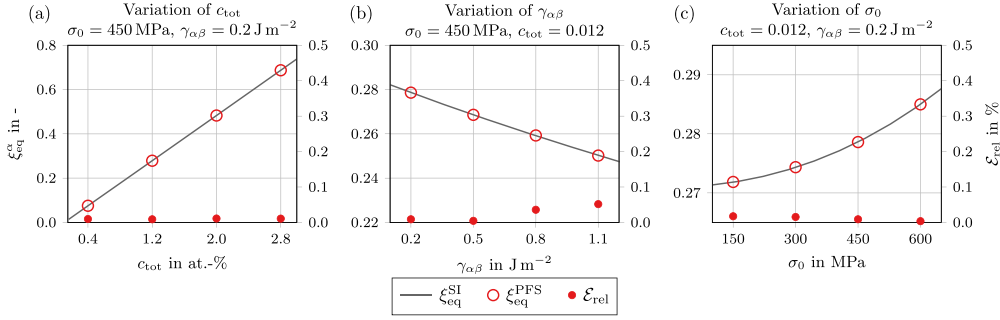
Figure 5. Benchmark II: the equilibrium phase fractions are compared while varying the total carbon concentration c_{tot} (a) and the surface energy $\gamma_{\alpha\beta}$ (b). The SI solutions are represented by solid lines and PFS results are represented by unfilled marks in (b). An increased surface energy results in a smaller equilibrium size of the inclusion.

investigated for different total concentrations c_{tot} and surface energies $\gamma_{\alpha\beta}$. The SI solution and the PFS results are visualized in figure 5. First of all, in figure 5(a) it can be seen that, analogous to the previous setup, the inclusion at equilibrium is larger for higher total concentrations. Moreover, it is visible, that a decreased surface energy $\gamma_{\alpha\beta}$ results in a bigger phase fraction of the inclusion in equilibrium. This becomes even clearer in figure 5(b). Here, the resulting equilibrium phase fractions ξ_{eq} are plotted against the surface energy $\gamma_{\alpha\beta}$. With an increased surface energy $\gamma_{\alpha\beta}$ the capillary driving force is increased which results in a smaller inclusion in equilibrium. The PFS results are in good agreement with the SI solution. The relative error of the predicted equilibrium phase fractions $\mathcal{E}_{\text{rel}}^{\text{PFS}}$ does not exceed 0.1%. The curvature minimizing effect introduced by the capillary driving forces predicted with the analytical sharp interface solution is represented accurately in the diffuse interface context. The advantage of validating different driving forces within a unified framework becomes clear. In contrast to the approach taken in [48], all benchmarks are based on the same chemical free energies. The chemical driving force depends on the concentration, in contrast to the fixed contribution considered in [31]. Furthermore, the inclusion is not fixed in size as in [37, 46]. Instead, the impact of total concentration c_{tot} and surface energy $\gamma_{\alpha\beta}$ on the driving forces, including the capillary driving force, that result in different equilibrium sizes of the inclusion can be evaluated within a single benchmark.

Benchmark III.a — chemical, capillary, and mechanical driving forces. In this last benchmark, chemical, capillary, and mechanical driving forces are accounted for increasing the complexity of the benchmark, as introduced in Setup III, cf section 3.3. The formulation of mechanical boundary conditions is schematically depicted in figure 3. The mechanical boundary condition is formulated in terms of the plate dimensions L and is implemented as Dirichlet boundary conditions, cf equation (43). A study has been conducted by separately varying the total carbon concentration c_{tot}, the surface energy $\gamma_{\alpha\beta}$, and the boundary stress σ_0. The resulting phase fractions ξ_{eq}^{α} in equilibrium are depicted in figure 6 and correspond to the left ordinate. This setup resembles the mechanical solution derived in [61] and a very good alignment of the PFS

Figure 6. Benchmark III.a: the equilibrium phase fractions are compared with variation of the total concentration c_{tot} (a), the surface energy $\gamma_{\alpha\gamma}$ (b), and the boundary stress σ_0 (c) corresponding to the left ordinate. The SI solution is represented by a solid line, while PFS results and errors are represented by unfilled and filled marks, respectively. The evaluation of the relative error $\mathcal{E}_{\text{rel}}$ of the equilibrium volume is represented with respect to the right ordinate.

and the SI solution is visible. A detailed comparison of the stress and strain fields of one simulation can be found in appendix B. Moreover, for each PFS result in figure 6, the profiles of the concentration $\bar{c}$ and the order parameter ϕ_α are depicted in appendix B. The comparison of the equilibrium phase fractions reveals that the relative error of the PFS with respect to the SI solution $\mathcal{E}_{\text{rel}}$ does not exceed 0.1%. With increasing total carbon concentration c_{tot} the phase fraction of the austenitic inclusion increases linearly. With increasing surface energy $\gamma_{\alpha\beta}$ the inclusion is smaller in equilibrium due to the capillary driving force as elucidated in the previous section. The total bulk driving force is quadratic in the boundary stress σ_0, cf equation (45). Thus, with increasing stress the inclusion size increases quadratically. Within the chosen setup and especially with the selected alloy and temperature, cf table 1, the chemical driving force is dominating. Along with the impact of chemical and capillary driving forces, the impact of elastic energy on the equilibrium concentration is validated in a single setup, which differs from the approach taken in [40], where the effect was not considered. With the proposed benchmarks, the alteration of a single parameter results in different driving forces and ultimately different equilibrium stages, without necessitating a modification to the benchmark setup.

Benchmark III.b — comparison of different homogenization schemes within the diffuse interface region. The benchmark introduced in the previous paragraph is used to evaluate the performance and implementation of different homogenization schemes within the diffuse interface. In the following, three different homogenization schemes (VT, RS, and Jump) are discussed and the results are depicted in figure 7. It is clearly visible, by examination of the relative errors $\mathcal{E}_{\text{rel}}$ that the equilibrium phase fractions ξ_{eq} obtained with the jump condition approach are closest to the SI solution. The relative error $\mathcal{E}_{\text{rel}}$ of the RS and VT homogenization is approximately constant while varying the total concentration c_{tot} in figure 7(a) and the surface energy $\gamma_{\alpha\beta}$ in figure 7(b), since the mechanical driving force is constant in these cases. The relative error obtained comparing RS and VT with the SI solution increases with increasing mechanical contribution, i.e. increasing boundary stress σ_0, as visible in figure 7(c). With the use of RS and VT, an excess energy is introduced into the diffuse interface area. The sharp interface solution is not recovered as accurate as with the jump condition approach.
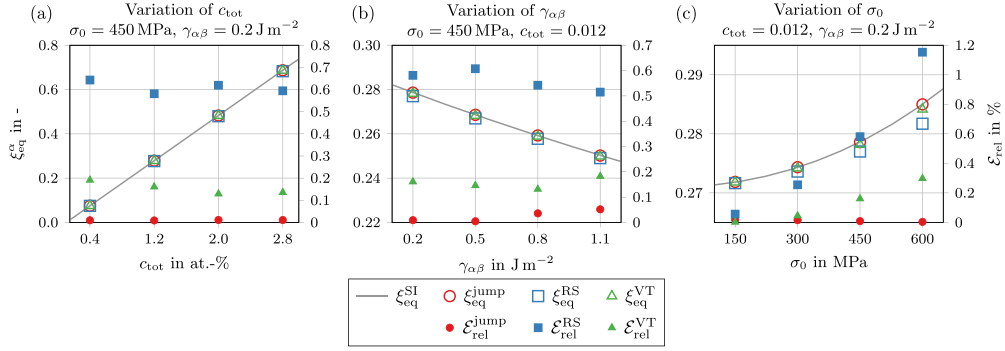
Figure 7. Benchmark III.b: different stress formulation within the diffuse interface are compared by means of equilibrium phase fractions (left ordinate) with variation of the total concentration c_{tot} (a), the surface energy $\gamma_{\alpha\beta}$ (b), and the boundary stress σ_0 (c). The relative error $\mathcal{E}_{\text{rel}}$ of the equilibrium phase fraction is evaluated corresponding to the right ordinate. The SI solution is represented by a solid line, while PFS results and errors are represented by unfilled and filled marks, respectively.
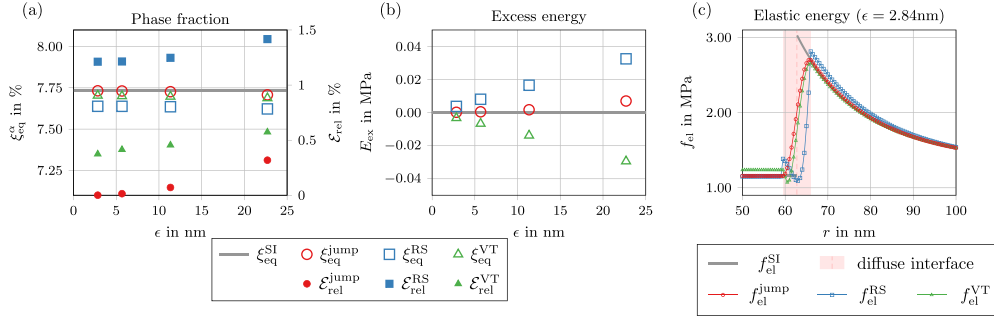
Figure 8. Benchmark III.b: the impact of the interface thickness is compared using different homogenization schemes within the diffuse interface. The phase fractions and their relative error ($\mathcal{E}_{\text{rel}}$) compared to the analytical solution of the sharp interface (SI) are depicted in (a) and the excess energy in (b). The SI solution is represented by a solid line, while PFS results and errors are represented by unfilled and filled marks, respectively.

This is highlighted by a study on the interfacial width, cf figure 8. Herein, the discretization is varied with $\Delta x \in [4, 2, 1, 0.5]$ nm with a constant length of the domain $L = 400$ nm and a constant number of cells in the interface $n_{\text{I}} = 14$. With a decreasing interface width the error decreases for all three homogenization approaches, cf figure 8(a). In figure 8(b) the excess energy $E_{\text{ex}} = \int_S f_{\text{el}}^{\text{SI}} - f_{\text{el}}^{\text{PFS}} \, \mathrm{d}S$ computed along the interface normal direction is displayed, which decreases with decreasing interface width. The jump condition approach is closest to the analytical solution even for very large interfaces. Here only a small error is introduced due to coarse discretization. With the RS and VT homogenization the elastic energy density f_{el} deviates from the analytical solution, resulting in a larger relative error of the phase fraction. This is caused by excess energy which is introduced mainly in the interface region

cf figure 8(c). A more detailed comparison can be found in [30]. With the proposed benchmark, advantages and disadvantages of different homogenization schemes within the diffuse interface region can be highlighted.

5. Conclusion

Summary. A set of three benchmarks has been proposed for the validation of chemical, capillary, and mechanical driving forces, in a weakly coupled chemo-elastic phase-field approach based on the grand potential density. Within this work, a two-component and two-phase approach has been considered. To quantify chemical free energies a CALPHAD database has been utilized. Phase-field simulation results are compared with an analytical solution derived on basis of the generalized Gibbs-Thomson equation. The impact of each driving force is examined separately and in combination with the use of a series of chemo-elastic equilibrium states for Fe-C binary alloys. Despite their success, these benchmarks constitute a relatively simple approach that should act as a foundational starting point for more complex extensions.

Extensions. Future work may focus on enhancing the benchmarks' complexity and applying them to more complex scenarios like multi-component, multi-phase, and chemo-mechanically fully coupled systems. In this work, a chemo-mechanically weakly coupled phase-field model is considered. Nevertheless, the set of benchmarks is readily adaptable to a fully coupled model. In the weakly coupled case, the diffusion potential is given by the chemical potential, i.e. $\mu = \mu_{\text{chem}}$, providing an invertible expression for the concentration. In the fully coupled case, the diffusion potential is composed of a chemical and an elastic potential, i.e. $\mu = \mu_{\text{chem}} + \mu_{\text{el}}$, with $\mu_{\text{el}} := \partial f_{\text{el}}/\partial c$. In this case, it might be convenient to formulate the equilibrium conditions on the driving force and the diffusion potential directly in terms of the concentrations c_α and c_β

$$\{f_{\text{chem}}\}^{\alpha\beta} - \mu_{\text{chem}}^\alpha \{c\}^{\alpha\beta} + 2\bar{\kappa}_{\mathcal{S}}\gamma_{\alpha\beta} + \{f_{\text{el}}\}^{\alpha\beta} - \mu_{\text{el}}^\alpha \{c\}^{\alpha\beta} - \bar{\sigma} \cdot \{\varepsilon\}^{\alpha\beta} = 0 \tag{46}$$

$$\mu_{\text{chem}}^\alpha (c_\alpha) + \mu_{\text{el}}^\alpha (c_\alpha) = \mu_{\text{chem}}^\beta (c_\beta) + \mu_{\text{el}}^\beta (c_\beta) . \tag{47}$$

The equilibrium conditions are solved for the equilibrium concentrations c_α and c_β. For comparison with the weakly coupled model see equations (39) and (5). The dependency of the elastic free energy on the concentration can be modeled, e.g. in terms of concentration dependent eigenstrains or elastic moduli. Moreover, alternative mechanical BVPs, e.g. which may include (concentration dependent) eigenstrains, can be considered by applying the respective analytical solutions in the equilibrium condition. Moreover, the straightforward design of the benchmarks allows for the incorporation of additional driving forces with very little effort. The extension of the presented set of benchmarks to enable their use in validating multiphase problems with junctions involving multiple phases necessitates the development of a new setup.

Conclusion. The simplicity of the current benchmarks allows for clear and concise validation, ensuring that the basic principles and interaction of diffusive, displacive, and curvature driven forces are accurately represented. It is our intention that the proposed set of benchmarks will serve the scientific community in order to facilitate future model developments and help to solidify the chemo-mechanical phase-field approach as a versatile and powerful tool in computational materials science.

Data availability statement

The manuscript is written in such a way that no additional data is required. The data presented are reproducible based on the information provided in the manuscript. The data that support the findings of this study are available upon reasonable request from the authors.

## Appendix A. Accuracy of approximated Gibbs energy functions

The accuracy of the approximations of the Gibbs energy functions depends on the considered temperature and concentration ranges [55]. In the present work, the equilibrium calculations proposed necessitate a good approximation in the vicinity of equilibrium concentrations. In this limited range, the use of quadratic functions provides a sufficient approximation and enables an efficient computation. An advantage of employing parabolic functions is the straightforward derivation of an invertible expression between the composition and the chemical potential, which is a necessary condition within the grand potential approach. Alternative fitting functions are summarized, e.g. by Noubary *et al* [55]. The accuracy of the approximation can be evaluated by comparing the equilibrium concentrations calculated based on the sharp interface (SI) solution and equilibrium calculations using the Thermo-Calc software (TC) [54] as reported in table A1. Since the equilibrium carbon concentration of ferrite is very close to zero, the fit is slightly less accurate than for austenite. However, this results in a maximum absolute error $\mathcal{E}_{\text{abs}} = |\xi_{\text{eq}}^{\text{TC}} - \xi_{\text{eq}}^{\text{SI}}| \approx 0.33\%$ when comparing the phase fractions obtained with TC and SI, indicating a high precision of the analytic solution derived using parabolic approximations in the sharp interface context. This justifies the use of the coefficients in table 1.

Table A1. Equilibrium concentrations obtained within the Thermo-Calc Software using the TCFE7 thermodynamic database (TC) and based on sharp interface solution based on parabolic approximation (SI) are compared by means of the relative error $\mathcal{E}_{\text{rel}}$.

	$c_{\text{eq}}^{\text{TC}}$ in at.-%	$c_{\text{eq}}^{\text{SI}}$ in at.-%	$\mathcal{E}_{\text{rel}}$ in %
Austenite	4.0934	4.0804	0.3176
Ferrite	0.0974	0.0931	4.4148

Appendix B. Detailed evaluation

In figure B1, the stress and strain components $\bar{\sigma}_{\text{xx}}$, $\bar{\sigma}_{\text{yy}}$, $\bar{\varepsilon}_{\text{xx}}$, and $\bar{\varepsilon}_{\text{yy}}$ are depicted for both SI (first row) and PFS (second row). Additionally, their profiles along the indicated horizontal
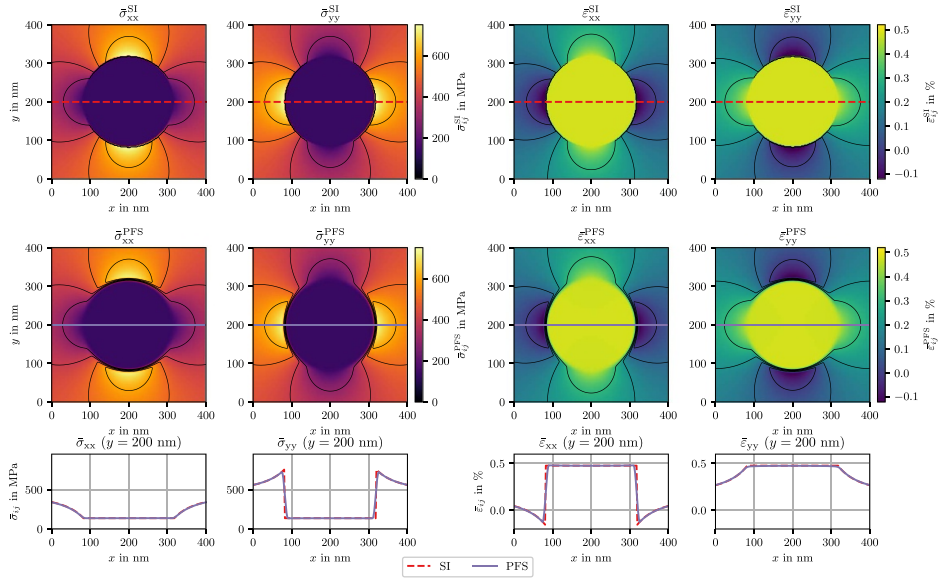
Figure B1. Comparison of stress and strain fields $\bar{\sigma}_{xx}$, $\bar{\sigma}_{yy}$, $\bar{\varepsilon}_{xx}$, and $\bar{\varepsilon}_{yy}$ for $c_{tot} = 1.2$ at.-%, $\gamma_{\alpha\beta} = 0.4\,\mathrm{J\,m}^{-2}$, and $\sigma_0 = 450\,\mathrm{MPa}$. The first and second rows depict the SI and PFS results, respectively. The third row depicts the corresponding profiles along the indicated horizontal lines.
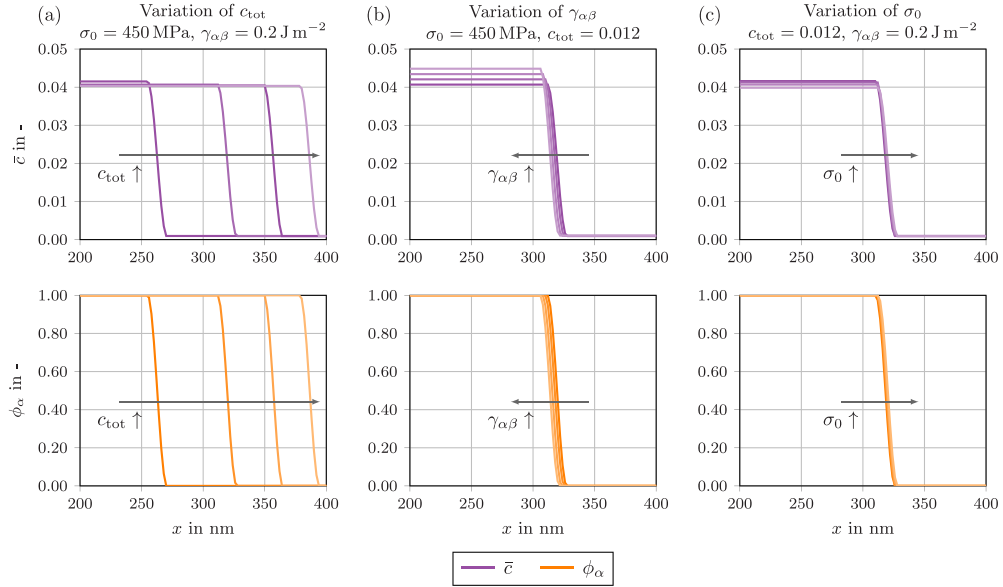
Figure B2. Profiles of the concentration $\bar{c}$ (first row) and the order parameter ϕ_α (second row). Each profile corresponds to a PFS result depicted in figure 6.

lines are compared in the last row. It is readily apparent, that the PFS results match the SI solutions very well. Additionally, it is clear to see, that no boundary effects are introduced with the mechanical boundary conditions, as the SI solution for the displacement is directly imposed on the boundary, in contrast to the benchmarks in [37, 46]. This is also evident in figure B2, where the profiles for the concentration $\bar{c}$ (first row) and the order parameter ϕ_α (second row) are depicted. Each profile in figure B2 corresponds to a PFS result depicted in figure 6. Even for very large inclusions, the profiles are not distorted. When phase fractions are similar, the profiles of both concentrations and order parameters exhibit minimal discrepancy, which is why the PFS and SI results are compared in terms of the equilibrium phase fraction.

ORCID iDs

Thea Kannenberg ⓘ https://orcid.org/0009-0002-5243-5164
Andreas Prahs ⓘ https://orcid.org/0000-0002-8112-9994
Bob Svendsen ⓘ https://orcid.org/0000-0002-1519-9433
Britta Nestler ⓘ https://orcid.org/0000-0002-3768-3277
Daniel Schneider ⓘ https://orcid.org/0000-0002-9250-2918

References

[1] Chen L-Q 2002 *Annu. Rev. Mater. Res.* **32** 113–40
[2] Moelans N, Blanpain B and Wollants P 2008 *Calphad* **32** 268–94
[3] Steinbach I 2009 *Modelling Simul. Mater. Sci. Eng.* **17** 073001
[4] van der Waals J D 1894 *Z. Phys. Chem.* **13U** 657–725
[5] Ginzburg V L 1955 *Nuovo Cimento* **2** 1234–50
[6] Cahn J W and Hilliard J E 1958 *J. Chem. Phys.* **28** 258–67
[7] Kobayashi R 1993 *Physica* D **63** 410–23
[8] Steinbach I, Pezzolla F, Nestler B, Seeßelberg M, Prieler R, Schmitz G and Rezende J 1996 *Physica* D **94** 135–47
[9] Steinbach I and Pezzolla F 1999 *Physica* D **134** 385–93
[10] Nestler B, Garcke H and Stinner B 2005 *Phys. Rev.* E **71** 041609
[11] Khachaturyan A G 1983 *Theory of Structural Transformations in Solids* (Wiley)
[12] Svendsen B, Shanthraj P and Raabe D 2018 *J. Mech. Phys. Solids* **112** 619–36
[13] Lv S, Wang S, Wu G, Gao J, Yang X, Wu H and Mao X 2022 *J. Iron Steel Res. Int.* **29** 867–80
[14] Yamanaka A 2023 *ISIJ Int.* **63** 395–406
[15] Amos P G, Schoof E, Schneider D and Nestler B 2018 *J. Alloys Compd.* **767** 1141–54
[16] Cottura M, Appolaire B, Finel A and Le Bouar Y 2015 *Scr. Mater.* **108** 117–21
[17] Eiken J, Böttger B and Apel M 2023 *IOP Conf. Ser.: Mater. Sci. Eng.* **1281** 012051
[18] Shchyglo O, Du G, Engels J K and Steinbach I 2019 *Acta Mater.* **175** 415–25
[19] Salama H, Ali M A, Shchyglo O and Steinbach I 2024 *Comput. Mater. Sci.* **241** 113033
[20] Düsing M and Mahnken R 2019 *Int. J. Solids Struct.* **162** 45–59
[21] Schoof E, Kubendran Amos P, Schneider D and Nestler B 2020 *Materialia* **9** 100620
[22] Böttger B, Apel M, Budnitzki M, Eiken J, Laschet G and Zhou B 2020 *Comput. Mater. Sci.* **184** 109909
[23] Cottura M, Appolaire B, Finel A and Le Bouar Y 2021 *Acta Mater.* **212** 116851
[24] Ali M A, Shchyglo O, Stricker M and Steinbach I 2023 *Comput. Mater. Sci.* **220** 112069
[25] Wang Z, Jiang W, Zhao Y, Hu L, Wang Y and Ma Z 2023 *J. Solid State Electrochem.* **27** 245–53
[26] Daubner S *et al* 2024 *npj Comput. Mater.* **10** 75
[27] Ammar K, Appolaire B, Cailletaud G and Forest S 2009 *Eur. J. Comput. Mech.* **18** 485–523
[28] Durga A, Wollants P and Moelans N 2013 *Modelling Simul. Mater. Sci. Eng.* **21** 055018
[29] Mosler J, Shchyglo O and Hojjat H M 2014 *J. Mech. Phys. Solids* **68** 251–66
[30] Schneider D, Tschukin O, Choudhury A, Selzer M, Böhlke T and Nestler B 2015 *Comput. Mech.* **55** 887–901
[31] Kiefer B, Furlan T and Mosler J 2017 *Int. J. Numer. Methods Eng.* **112** 1097–128

[32] Silhavy M 1997 *The Mechanics and Thermodynamics of Continuous Media* (Springer)

[33] Wheeler A A, Boettinger W J and McFadden G B 1992 *Phys. Rev.* A **45** 7424–39

[34] Kim S G, Kim W T and Suzuki T 1999 *Phys. Rev.* E **60** 7186–97

[35] Plapp M 2011 *Phys. Rev.* E **84** 031601

[36] Choudhury A and Nestler B 2012 *Phys. Rev.* E **85** 021602

[37] Simon P C A, Aagesen L K, Motta A T and Tonks M R 2020 *Comput. Mater. Sci.* **183** 109790

[38] Daubner S, Hoffrogge P W, Minar M and Nestler B 2023 *Comput. Mater. Sci.* **219** 111995

[39] Schneider D, Schwab F, Schoof E, Reiter A, Herrmann C, Selzer M, Böhlke T and Nestler B 2017 *Comput. Mech.* **60** 203–17

[40] Kamachali R D, Schwarze C, Lin M, Diehl M, Shanthraj P, Prahl U, Steinbach I and Raabe D 2018 *Comput. Mater. Sci.* **155** 541–53

[41] Jokisaari A, Voorhees P, Guyer J, Warren J and Heinonen O 2017 *Comput. Mater. Sci.* **126** 139–51

[42] Eiken J 2020 *ISIJ Int.* **60** 1832–4

[43] Minar M and Moelans N 2022 *Phys. Rev. Mater.* **6** 103404

[44] Jokisaari A, Voorhees P, Guyer J, Warren J and Heinonen O 2018 *Comput. Mater. Sci.* **149** 336–47

[45] Cahn J and Larché F 1984 *Acta Metall.* **32** 1915–23

[46] Durga A, Wollants P and Moelans N 2015 *Comput. Mater. Sci.* **99** 81–95

[47] Bai Y, Mianroodi J R, Ma Y, da Silva A K, Svendsen B and Raabe D 2022 *Acta Mater.* **231** 117899

[48] Tschukin O, Schneider D and Nestler B 2019 *Eur. J. Mech.* A **73** 181–91

[49] Hakala R W 1952 *J. Chem. Educ.* **29** 453

[50] Hoffrogge P W, Daubner S, Schneider D, Nestler B, Zhou B and Eiken J 2025 *Modelling Simul. Mater. Sci. Eng.* **33** 015001

[51] Goldstein H, Poole C P and Safko J L 2002 *Classical Mechanics* 3rd edn (Addison Wesley)

[52] Eiken J, Böttger B and Steinbach I 2006 *Phys. Rev.* E **73** 066122

[53] Hoffrogge P W, Mukherjee A, Nani E S, Amos P G K, Wang F, Schneider D and Nestler B 2021 *Phys. Rev.* E **103** 033307

[54] Andersson J-O, Helander T, Höglund L, Shi P and Sundman B 2002 *Calphad* **26** 273–312

[55] Noubary K D, Kellner M, Hötzer J, Seiz M, Seifert H J and Nestler B 2021 *J. Mater. Sci.* **56** 11932–52

[56] Schneider D, Schoof E, Tschukin O, Reiter A, Herrmann C, Schwab F, Selzer M and Nestler B 2017 *Comput. Mech.* **61** 277–95

[57] Johnson W C and Alexander J I D 1986 *J. Appl. Phys.* **59** 2735–46

[58] Voorhees P W and Johnson W C 1986 *J. Chem. Phys.* **84** 5108–21

[59] Cermelli P, Fried E and Gurtin M E 2005 *J. Fluid Mech.* **544** 339

[60] Hötzer J, Reiter A, Hierl H, Steinmetz P, Selzer M and Nestler B 2018 *J. Comput. Sci.* **26** 1–12

[61] Mal A K 1991 *Deformation of Elastic Solids* (Prentice Hall)